Geochemistry, Geophysics, Geosystems

RESEARCH ARTICLE
10.1029/2019GC008744

Scales of Stress Heterogeneity Near Active Faults in the Santa Barbara Channel, Southern California

Patricia Persaud[1], Edward H. Pritchard[1,2], and Joann M. Stock[3]

[1]Department of Geology and Geophysics, Louisiana State University, Baton Rouge, LA, USA, [2]Credit Suisse, Houston, TX, USA, [3]Seismological Laboratory, California Institute of Technology, Pasadena, CA, USA

Key Points:
- New forward modelling technique gives orientations and relative magnitudes of the principal stresses from breakouts in deviated boreholes
- Short-length scale stress heterogeneity (less than 10 km laterally and 1 km in depth) exists in the Santa Barbara Channel
- Variations in maximum principal stress orientation coincide with changes in fault geometry and may have implications for seismic hazard

Correspondence to:
P. Persaud,
ppersaud@lsu.edu

Citation:
Persaud, P., Pritchard, E. H., & Stock, J. M. (2020). Scales of stress heterogeneity near active faults in the Santa Barbara Channel, Southern California. *Geochemistry, Geophysics, Geosystems*, *21*, e2019GC008744. https://doi.org/10.1029/2019GC008744

Received 30 SEP 2019
Accepted 30 DEC 2019
Accepted article online 3 JAN 2020

Abstract The Santa Barbara Channel represents the offshore portion of the Ventura Basin in Southern California. Ongoing transpression related to a regional left step in the San Andreas Fault has led to the formation of E-W trending en-echelon fault systems that accommodate localized shortening across the basin. Recent studies have suggested that faults within the channel could be capable of a multisegment rupture and producing a M_w 7.7–8.1 tsunamigenic earthquake. However, dynamic rupture models producing these results do not account for stress heterogeneity. With only sparse information available on the stress field in this region, further borehole-derived stress constraints are essential for obtaining a more comprehensive understanding of the hazards related to the complex fault systems. We used caliper logs from 19 wells obtained from industry to identify stress-induced borehole breakouts beneath the Holly and Gail oil platforms in the channel. Our newly developed forward modeling technique provides constraints on the orientations and relative magnitudes of the three principal stresses. At Gail, we determine a reverse faulting stress regime ($S_{Hmax} = 1.7$; $S_{hmin} = 1.6$; $S_V = 1.0$) and an S_{Hmax} azimuth of N45°E. Our results are consistent with local structures, which reflect deeper regional scale trends, and with similar studies onshore nearby. At Holly, an S_{Hmax} rotation from ~N36°W to ~N57°E occurs across ~100 m depth in a single well and differs from nearby results, indicating that short-length scale (<10 km laterally and <1 km in depth) stress heterogeneity is associated with complex changes in fault geometry.

Plain Language Summary Studies have suggested that faults within the Santa Barbara Channel in Southern California could be capable of producing a Mw 7.7–8.1 earthquake and tsunami, which would pose a major hazard to nearby populated areas. Information on the stress field in this region is one of the key ingredients needed to produce realistic computer models that allow us to determine the likelihood of a large earthquake rupture occurring and to estimate the ground motions that could result from such rupture. We use oil industry data from 19 boreholes drilled beneath the Santa Barbara Channel to provide information on the stress field for earthquake hazard purposes. We addressed the challenge of working with boreholes that are not drilled straight down into the earth but have complex paths by comparing our data to theoretical predictions. We find that the stress field is more complex and variable than previously documented with important changes in the stress field occurring across short distances of just a few kilometers. These changes coincide with changes in the geometry of the major fault systems and may lead to a reevaluation of whether multiple faults are likely to connect up to produce a large earthquake rupture in this region.

1. Introduction

The Transverse Ranges province (Figure 1a) is a major structural and geomorphic province in Southern California characterized by its east-west trending anticlinal mountain ranges and synclinal basins, which interrupt the dominant northwest structural grain of the rest of the state (Hadley & Kanamori, 1977; Vedder et al., 1969). The westernmost extent of this province is the Santa Barbara Channel (Figure 1), an east-west trending tectonic depression and the offshore westward continuation of the Ventura Basin (Vedder et al., 1969). Rapid tectonic convergence (~2.5-7 mm/yr) in the greater Ventura region [*S* Marshall et al., 2013] has led to elevated background seismicity with low magnitude earthquake swarms, for example, the 2015 Fillmore swarm (>1400 events of M ≥ 0.0, maximum M2.8), the 1968 swarm of 62 earthquakes in the Santa Barbara Channel (maximum M5.2), and several moderate to large events including the 1812 M > 7 earthquake, the 1925 M6.3, the 1941 M5.9, and the 1978 M_L 5.1 earthquakes [Hauksson et al., 2016; *S* Marshall et al., 2013; Sorlien & Kamerling, 2000; Sylvester et al., 1970; Wallace et al., 1981].

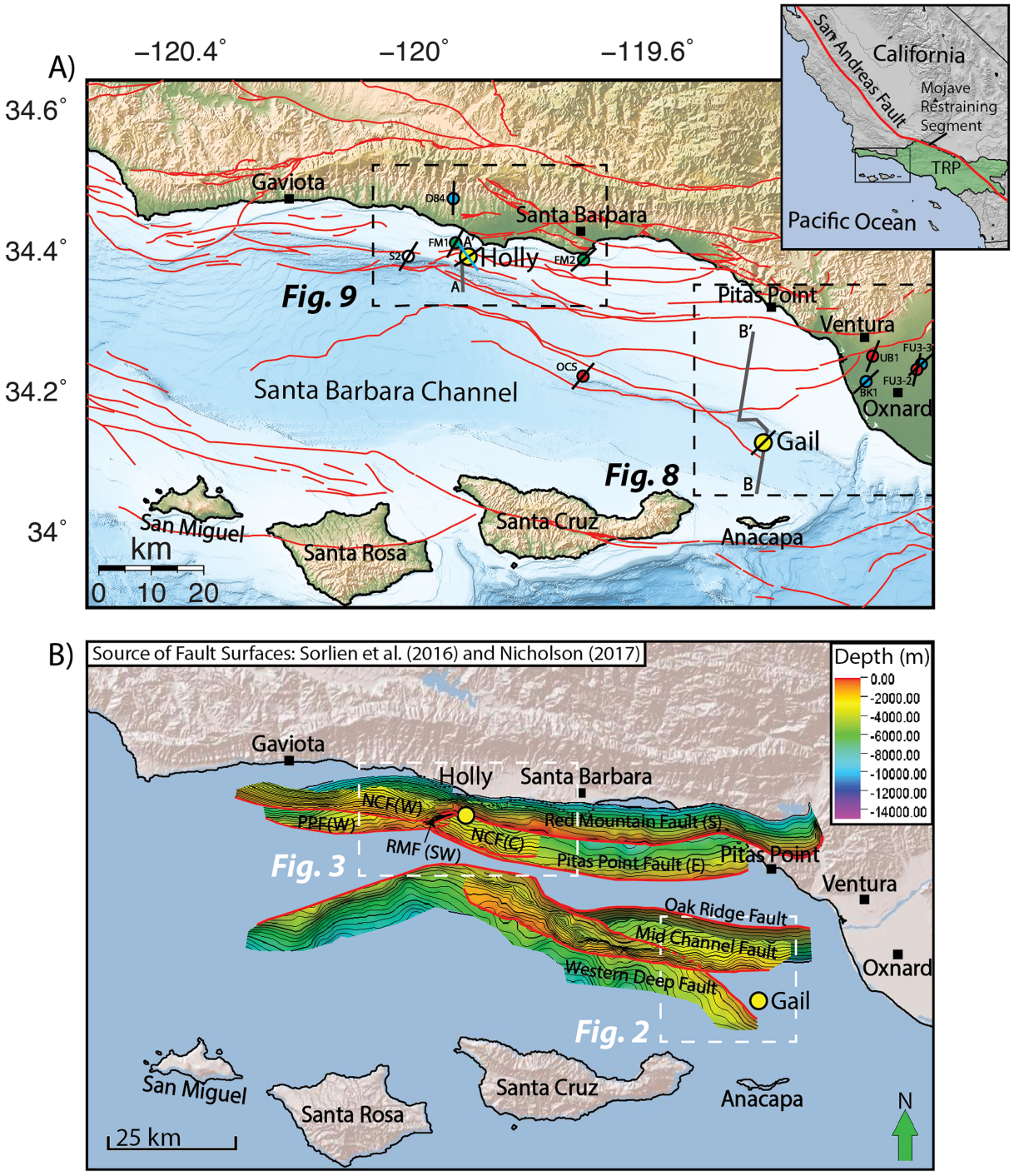

Figure 1. (a) Map of the Santa Barbara Channel showing the locations of platforms Holly and Gail (yellow circles), the Heck and Edwards (1998) well (white circle), the Wilde and Stock (1997) wells (blue circles), the Mount and Suppe (1992) wells (red circles), and the two World Stress Map single earthquake focal mechanisms (FM1 and FM2) (green circles) (Heidbach et al., 2010). S_{Hmax} orientations are shown with black lines, and the blue line at platform Holly represents S_{Hmax} at 557–568 m TVD. Red lines onshore are Quaternary faults (Jennings & Bryant, 2010), offshore red lines are fault traces from Sorlien et al. (2016), black dashed boxes represent the extents of Figures 8 and 9, and grey lines represent the locations of the 2-D seismic reflection lines A–A′ and B–B′. Inset map shows the Santa Barbara Channel outlined with a black box. The Transverse Ranges Province (TRP) is shown with green shading. The digital elevation model was obtained from Divins, D. L., and D. Metzger, NGDC Coastal Relief Model, Retrieved date October 20, 2018 http://www.ngdc.noaa.gov/mgg/coastal/coastal.html. (b) Regional fault surfaces in the Santa Barbara Channel (Nicholson, 2017; Sorlien et al., 2016). The upper tips of the faults are traced with a red line. White dashed boxes represent the extents of Figures 2 and 3.

Repeated 6–8 m marine uplift terraces at Pitas Point, just west of Ventura (Figure 1), have been cited as evidence that damaging ~M_w 8.0 earthquakes have occurred in the western Transverse Ranges at a recurrence interval of 1–2 ka, with the last event occurring ~950 years ago (Rockwell et al., 2014). Hubbard et al. (2014) produced a fault representation of the onshore Ventura fault that shows it as structurally linked at depth with the Pitas Point and San Cayetano faults, forming a single continuous fault surface of >100 km length, which they believe may be capable of a massive, multisegment rupture, and producing a M_w 7.7–8.1 tsunamigenic earthquake. Dynamic rupture models based on the fault representations from Hubbard et al. (2014) that incorporate regional stress by applying a single, homogeneous stress regime and orientation to the entire fault system have supported these claims (Ryan et al., 2015). However, the fault representations of Hubbard et al. (2014) were created by extrapolating onshore fault geometries 30 km into the offshore basin, and it has been noted that a more complete understanding of the complex offshore fault geometries and segment boundaries, as well as the nature of slip across them would be beneficial to any assessment of the probability of multisegment earthquakes in this region (Sorlien & Nicholson, 2015). In addition, spontaneous rupture models with self-similar heterogeneous initial stresses on a fault have shown complex rupture behaviors such as jumped or triggered ruptures and delayed or paused ruptures, and the directivity effect on peak ground velocity may be significantly reduced for self-similar heterogeneous stresses (Liu & Duan, 2018).

Although the scales of stress heterogeneities are not the same everywhere, various studies have indicated that the local stress field near earthquake faults is not homogenous (e.g., Rivera & Kanamori, 2002) and likely varies substantially, especially at geometric complexities such as step-overs or bends (Liu et al., 2016). Furthermore, studies of model sensitivity to changes in stress inputs have indicated that increased stress heterogeneity tends to produce shorter rupture lengths (Lozos et al., 2015), and minor rotations of the orientation of maximum compressive stress (30°) can reduce calculated peak ground velocities by over 40% (Roten et al., 2014). Only a few constraints on stress orientations beneath the Santa Barbara Channel exist; still, previous studies have indicated that they are not uniform throughout the region (Mount & Suppe, 1992; Wilde & Stock, 1997). In this study, we use borehole breakouts to determine new stress constraints beneath two offshore oil platforms in the Santa Barbara Channel. Our results, when combined with those of previous borehole breakout studies in the region, provide insight into the scale at which breakouts record crustal stress, as well as the scale at which stress heterogeneity exists in the upper 1.8 km of crust beneath this region.

2. Background

2.1. Geological Setting of the Santa Barbara Channel

The Santa Barbara Channel exists in its present form as a result of Miocene extension followed by recent and ongoing transpression (Atwater, 1970; Atwater & Stock, 1998; Crouch & Suppe, 1993; Dickinson, 1996; Ingle, 1980; Kamerling & Luyendyk, 1985; Marshall, 2012; Nicholson et al., 1994; Seeber & Sorlien, 2000). Beginning in the late Oligocene to early Miocene, the ~90–100° clockwise rotation of the Western Transverse Ranges Province led to oblique rifting which formed the Santa Barbara-Ventura Basin (Atwater & Stock, 1998; Kamerling & Luyendyk, 1985; Marshall, 2012; Nicholson et al., 1994). This was followed by microplate capture and minor clockwise rotation of Baja California (Nicholson et al., 1994), which, when combined with a change in geometry and an eastward jump of the Pacific-North America plate boundary, initiated a transpressional regime across parts of Southern California and produced a collision across a regional scale left step in the San Andreas fault called the Mojave Restraining Segment or Big Bend (inset Figure 1a) [Ingle, 1980; Larsen et al., 1993; Larson & Webb, 1992; *C J* Marshall, 2012; Pinter et al., 1998]. Crustal contraction in the province was also due to crowding along the edges of rotating fault-bounded crustal blocks during the latter stages of clockwise transrotation along the borderland (e.g., Dickinson, 1996).

Regionally, this contraction led to rapid uplift of the Transverse Ranges and rapid subsidence of the synclinal Santa Barbara-Ventura Basin (Ingle, 1980; Larsen et al., 1993; Larson & Webb, 1992; Marshall, 2012; Pinter et al., 1998). Within the Santa Barbara Channel itself, normal and/or strike-slip faults that developed during Miocene extension were reactivated within an actively contracting fold-thrust belt (Shaw & Suppe, 1994; Sibson, 2004; Yeats et al., 1988). Currently, shortening across the basin is accommodated by several east-west trending en-echelon fault systems, with both north and south dips (Figure 1b), which transverse the north

and mid-channel regions, and control an overlying series of tight, asymmetric, anticlinal folds (Nicholson, 2017; Sorlien et al., 2016; Sorlien & Nicholson, 2015).

2.2. State of Stress in Southern California

Several previous studies have employed the use of various different stress indicators to provide constraints on crustal stress in Southern California. Yang and Hauksson (2013) inverted 179,000 high-quality earthquake focal mechanisms for earthquakes recorded from 1981 to 2010 and determined maximum horizontal compressive stress (S_{Hmax}) orientations and faulting styles across Southern California. Similar to Hardebeck and Hauksson (2001), they noted that the regional trend of S_{Hmax} in central to Southern California is generally NNE, with a most likely S_{Hmax} trend of N7°E. They also noted, however, that several regional and local stress heterogeneities exist at various spatial scales and degrees of heterogeneity, and transitions from one state of stress to another occur over distances of only a few kilometers. Similar local scale (<100 km) stress heterogeneities have been identified in other regions (e.g., Heidbach et al., 2010; Montone et al., 2012) and are believed to be controlled by phenomena such as active faulting, gravitational collapse, local intrusions, density and strength contrasts, basin geometry, topography and detachment faults (Heidbach et al., 2010; Yang & Hauksson, 2013).

Mount and Suppe (1992) observed borehole breakouts in 118 near-vertical wellbores in southwestern California and indicated that S_{Hmax} was generally oriented NE-SW, at a high angle to the San Andreas Fault. However, S_{Hmax} orientations from wellbores within individual basins differed as much as 50° from one another, and distinct rotations of S_{Hmax} were noted between basins, indicating both regional and local scale stress heterogeneities. Wilde and Stock (1997) observed borehole breakouts in 71 wellbores from six regions in Southern California west of the San Andreas Fault and similarly identified a generally NE-SW trend of S_{Hmax}, but also noted the presence of systematic variations in S_{Hmax} orientations both within and between individual basins that indicate strong heterogeneity in the stress field at shallow depths. They further noted the presence of anomalous NW directions of S_{Hmax} in certain regions, which they believe may be related to structural complexities of nearby fault systems.

2.3. State of Stress in the Santa Barbara Channel

Yang and Hauksson (2013) performed four independent 2-D stress inversions of focal mechanisms in Southern California at different spatial scales, two grid scales (5 km, 10 km), and with two numbers of events per grid node ($N = 30$, $N = 15$). They also performed a 3-D stress inversion with a 5-km scaled cubic grid and 30 events per grid node to examine stress field variations with depth. Their results indicate that the channel is dominated by reverse and strike-slip faulting regimes with considerable spatial heterogeneity between nearby areas. They also show significant heterogeneity in S_{Hmax} orientations, which range from roughly N10°W to N30°E. In comparison with the north Channel region, earthquake density near platform Gail is relatively low. However, at a grid scale of 10 km, and 15 events per grid node, focal mechanisms indicate the presence of a reverse faulting regime, with an S_{Hmax} orientation between N10°E and N20°E. At platform Holly, denser earthquake coverage allowed for constraint of the faulting style and S_{Hmax} orientation at a grid scale of 5 km and 30 earthquakes per grid node. Focal mechanism results indicate the presence of a reverse faulting regime near platform Holly, but the smaller, denser grid nodes show great heterogeneity in the orientation of S_{Hmax} in the very small area surrounding the platform. The 5 km × 5 km grid node in which Holly is located indicates an S_{Hmax} orientation between N20°E and N30°E. But platform Holly sits at the southern edge of this grid node, and the neighboring grid node to the south indicates an S_{Hmax} orientation of roughly N10°W. The 30–40° difference in S_{Hmax} orientation illustrates localized stress heterogeneity in the region near Holly.

Although borehole breakout studies in general indicate a NE-SW orientation of S_{Hmax} for Southern California, very few borehole breakout-derived stress constraints have been provided within the Santa Barbara Channel itself. Only one well from Mount and Suppe (1992) was located within the channel, OCS-P-0231 (OCS) (Figure 1a). Results from this well indicate an S_{Hmax} orientation of N49°E. Wilde and Stock (1997) examined 13 wells located within the channel, and these were actually drilled from platform Holly. However, these wells were highly deviated from the vertical, and breakouts occurring in them were not used to constrain the orientation of S_{Hmax}. Wilde and Stock (1997) instead applied to these wells an S_{Hmax} orientation of N2°E that was determined from the near-vertical Dreyfus #84 (D84) well (Figure 1a), which is located onshore and roughly 10 km north of Holly (Figure 1a). They also provided a rough

estimate of the best-fit theoretical stress state, performed by eye, and stated that the breakouts from deviated well sections at Holly represented a reverse faulting stress regime.

In addition to these two large-scale borehole breakout studies, Heck and Edwards (1998) also provided an estimate of S_{Hmax} from borehole breakouts in the Samedan #2 well of Gato Canyon lease 460 (S2 in Figure 1a), located ~10 km west of platform Holly, which indicated an S_{Hmax} orientation of N32°E. They also identified preferred fracture strike directions of N25°E and N55°W in this well, that they noted are subparallel and subperpendicular, respectively, to their S_{Hmax} direction of N32°E. Prior to the current study, only two borehole breakout derived stress constraints exist within the Santa Barbara Channel itself, and only one study has provided a rough estimate of the faulting regime from borehole breakouts. Here we focus on determining the orientation of maximum horizontal compressive stress and the stress regime beneath the Gail and Holly platforms in the channel.

2.4. Structural Setting of Platforms Gail and Holly

Platform Gail is located at approximately 34°7′N, 119°24′W (Figure 1) and targets the Sockeye anticline and oil field in the southeastern part of the Santa Barbara Channel. The platform sits just north of the S-dipping, NW-striking Western Deep fault, and south of the N-dipping, E-W striking Mid-Channel fault, which intersects at depth with the steeply S-dipping E-W striking Oak Ridge fault to the north (Figures 1b and 2c) (Nicholson, 2017; Sorlien et al., 2016). Of these faults, both the Western Deep and Mid-Channel faults are blind, with sea floor deformation expressed as extensive folding rather than fault offset (Figure 2) (Sorlien et al., 2016). On a more local scale, however, the shallow structure beneath platform Gail seems to be most consistent with that of the Western Deep fault. The Sockeye anticline structure is a broad, NW-trending, doubly plunging anticline bounded both to the north and southwest by S-dipping, NW-striking thrust faults (Figure 2b) (DOGGR, 1992; Sankur et al., 1990).

Platform Holly is located at approximately 34°23′N, 119°54′W (Figure 1) and targets the South Ellwood oil field located in the structurally complex northern part of the Santa Barbara Channel. This area is dominated by the N-dipping faults of the Pitas Point-North Channel-Red Mountain fault systems, segments of which extend 120 km west from Ventura (Figure 1b). The two deepest faults of this system, the Pitas Point and North Channel faults, are blind faults with surface deformation expressed as folding rather than fault offset (Figure 3c) (Sorlien & Nicholson, 2015). These two faults extend nearly the entire length of the channel, with few changes to their generally E-W strike. However, both faults show brief, but significant changes in orientation near platform Holly, where there is a segment boundary in the North Channel fault, and a 25° continuous right-stepping double-bend in the Pitas Point fault (Figures 3a and 3b) (Sorlien & Nicholson, 2015). Both of these faults briefly strike NW in this small area and then return to an E-W orientation as they extend westward. In this same area, there is also a change in strike of the much shallower Red Mountain fault, which offsets the sea floor in many locations (e.g., Figure 3c). Near platform Holly, the Red Mountain fault is split into two segments (Figure 3a). The Red Mountain (S) segment, located mostly east of Holly, strikes ~E-W, but the Red Mountain (SW) segment, located west of Holly, briefly strikes NE-SW before merging with the underlying blind faults to the west (Figure 3a) (Sorlien & Nicholson, 2015).

2.5. SCEC Community Stress Model

The Southern California Earthquake Center Community Stress Model (SCEC CSM) is a collaborative effort to provide improved constraints on the 4-D stress field in Southern California by merging together information from borehole measurements, focal mechanisms, GPS strain rates, paleo-slip indicators, topographic loading, geodynamic and earthquake cycle modeling and induced seismicity into a series of stress and stressing rate models (Hardebeck et al., 2012). The majority of data compiled in the SCEC CSM are derived from focal mechanism inversions and geodetic velocity-based strain rates. However, these methods rely on gridding and interpolation of data, which obscures small-scale heterogeneities (Luttrell & Hardebeck, 2017). On the other hand, several previous studies have noted that borehole breakouts are able to capture stress heterogeneities that occur laterally from well to well, or with depth within a single well. Furthermore, borehole breakouts are able to capture localized perturbations in the crustal stress field that result from faults, fractures, or rock strength and density contrasts (Carminati et al., 2010; Day-Lewis et al., 2010; Kerkela & Stock, 1996; Malinverno et al., 2016; Rajabi et al., 2017; Shamir & Zoback, 1992), thus capturing stress heterogeneities where other methods fall short. Breakouts are also able to provide information on stress in the

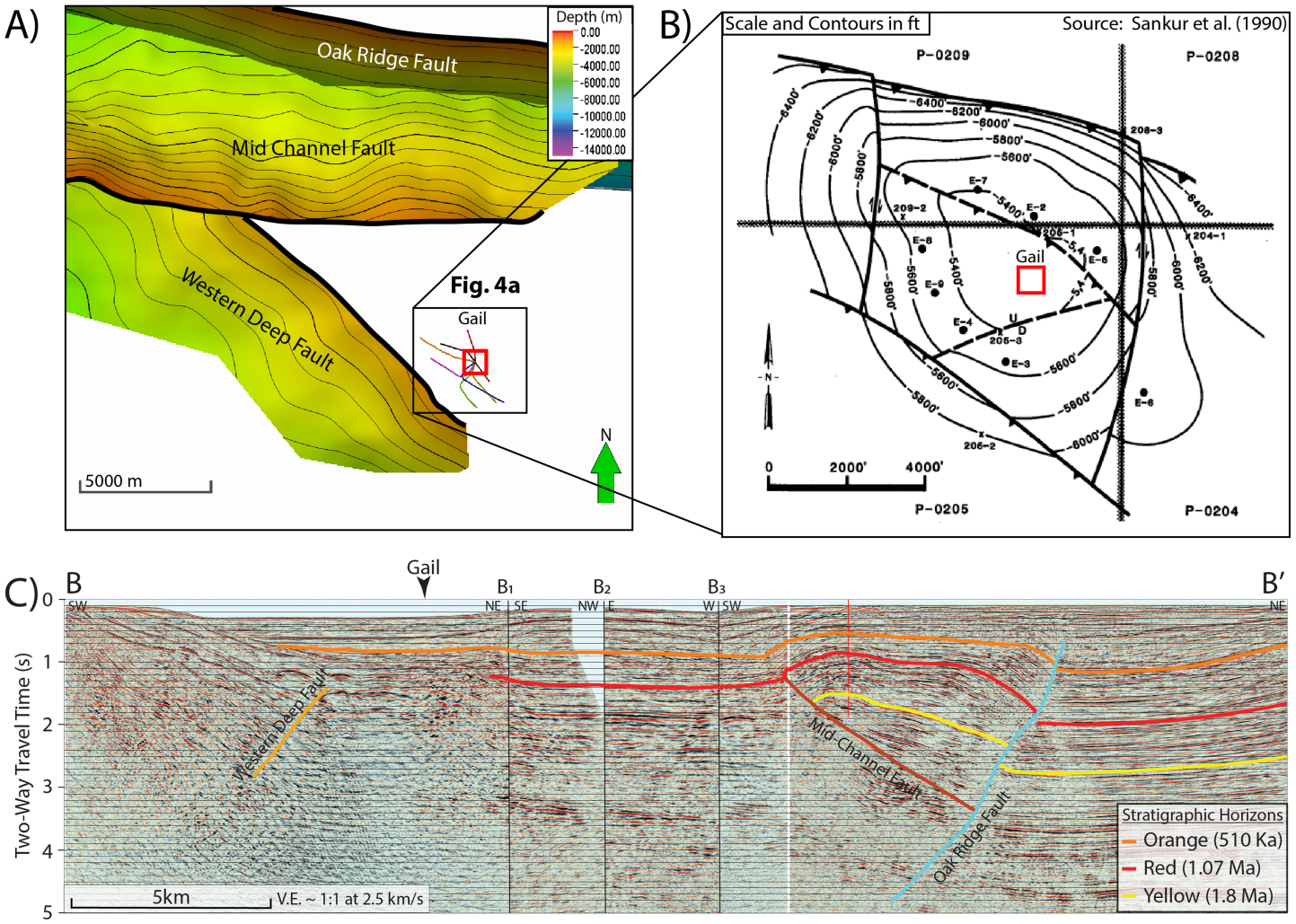

Figure 2. (a) View of platform Gail well paths from directly overhead showing the proximity of the platform to the NW-striking Western Deep Fault and the Mid-Channel fault. A closer view of the well paths is shown in Figure 4. Black lines mark the upper tips of the faults. (b) Contour map of the Sockeye Sespe unconformity from Sankur et al. (1990) showing the NW-trending Sockeye anticline structure, which is cut by NW-striking thrust faults that extend from at least 1.5–2 km depth towards the surface. Thick E-W and N-S lines are the boundaries of Outer Continental Shelf (OCS) leases 204, 205, 208, and 209 in the original figure in Sankur et al. (1990). (c) Composite 2-D seismic reflection profile with both stratigraphic (Behl et al., 2016) and fault interpretations (Sorlien & Nicholson, 2015). The profile runs roughly NE-SW with an ~5 km left step from B_1 to B_3 (see Figures 1a and 8 for profile location). Segment B–B_1 is 240 m west of platform Gail and shows the proximity of the platform to the Western Deep fault.

shallow (<5 km) and aseismic areas of the crust where focal mechanisms are less common, making them a valuable data source of the SCEC CSM.

3. Analysis of Borehole Breakout Data

When a wellbore is drilled, crustal stresses become concentrated in the wellbore wall as circumferential hoop stress. The maximum concentration of hoop stress occurs symmetrically on opposite sides of the wellbore, and when the magnitudes of these stresses exceed the strength of the rock, brittle shear failure occurs, forming spalled regions called borehole breakouts, which elongate the wellbore cross section into a roughly elliptical shape (e.g., Bell & Gough, 1979; Zoback, 2007).

In this study, we adhere to the common assumption that one of the principal stresses is vertical, and the other two principal stresses (S_{Hmax} and the minimum horizontal principal stress, S_{hmin}) therefore lie in the orthogonal horizontal plane (Bell, 1996; Peška & Zoback, 1995; Snee & Zoback, 2018; Zoback, 1992; Zoback et al., 2003). We, however, note that in structurally complex areas such as the western Transverse Ranges where oblique-slip faulting, inclined-axis fault-block rotations, and fault

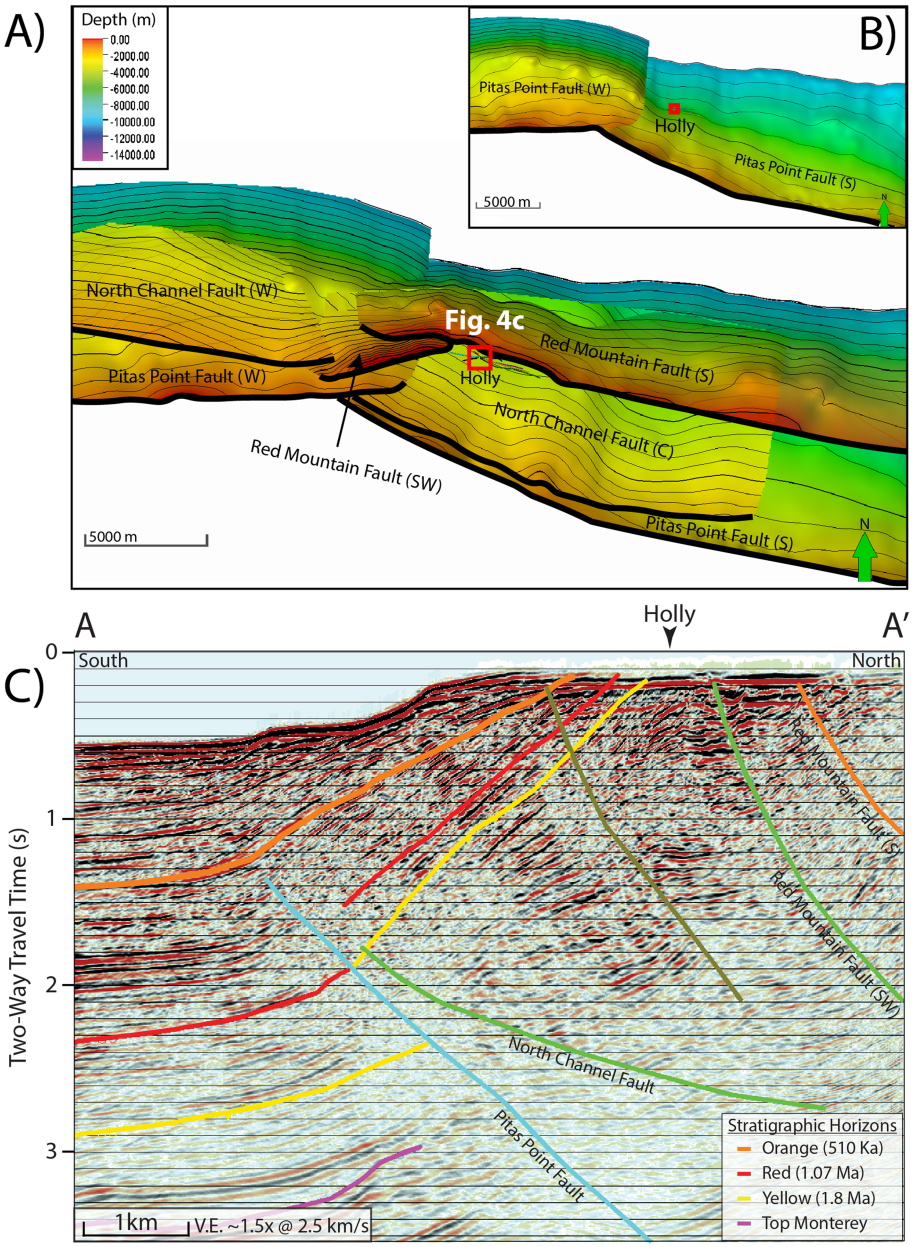

Figure 3. (a) View of platform Holly well paths from directly overhead showing the proximity of the platform to a structurally complex zone where the Pitas Point, North Channel, and Red Mountain faults all exhibit major changes in orientation. The wells are deviated primarily east and west from the platform and are shown in a larger map view in Figure 4. Black lines mark the upper tips of the faults. (b) View of platform Holly and the Pitas Point fault, which underlies segments of the North Channel and Red Mountain faults and strikes NW-SE beneath the platform due to an ~25° bend in its strike. (c) 2-D seismic reflection profile running N-S 1 km west of platform Holly with both stratigraphic (Behl et al., 2016) and fault interpretations (Sorlien & Nicholson, 2015). See Figures 1a and 9 for profile location. The profile shows the regional scale faults in close proximity to the platform including the Pitas Point, North Channel, Red Mountain (SW), and Red Mountain (S) faults. Both the Pitas Point and North Channel faults are blind, with upper tips at around 2 km depth sub-sea near platform Holly, but closer to the sea floor surface. The two steeply dipping segments of the Red Mountain Fault show offset of the sea floor within ~1 km of the platform.

interactions occur, non-vertical stress axes may be common. Indeed, Zajac and Stock (1997) have shown that removing the constraint of a vertical principal stress direction reduces the misfit between the theoretical stress state and the breakout data from the Siljan Deep Drilling Project in Sweden, and the Santa Maria basin, California has a stress state in which no principal stress is vertical. Relaxing

this assumption may thus reveal yet another aspect of stress field variability beyond that addressed in this study.

In deviated wellbores, the vertical principal stress is not oriented parallel to the wellbore and therefore contributes to the hoop stress. Thus, the position at which borehole breakouts form in non-vertical boreholes depends on the orientations and relative magnitudes of all three principal stress components, as well as the orientation of the wellbore itself (e.g., Qian & Pedersen, 1991). In an unchanging stress regime, the position at which borehole breakouts form varies systematically as wellbore orientation changes. Therefore, given enough closely spaced boreholes of varying orientations, we are able to determine the relative magnitudes and orientations of all three principal stress components.

3.1. Identification of Borehole Breakouts

We use oriented 4-arm caliper data recorded every 0.5 ft (0.1524 m) to identify and measure the orientations of borehole breakouts. A four-arm caliper tool records the diameter of the borehole along two coplanar axes, as well the orientation of a single reference pad, measured relative to both magnetic north (P1AZ), and to the high side of the borehole (relative bearing [RB]). As the caliper tool is pulled up a circular borehole, it rotates freely due to cable torque. However, in a breakout zone, two opposing arms of the caliper tool become stuck at the azimuth of borehole elongation if the breakout is wide enough, and rotation of the tool ceases. Thus, the orientation of borehole breakouts can be determined from the orientation of the stuck, elongated caliper arms. In order to distinguish borehole breakouts from other common borehole deformations and tool artifacts such as an off-center tool, we use the following borehole breakout selection criteria modified from Zajac and Stock (1997).

1. Tool rotation stops in the zone of elongation. At Gail, this is determined by limiting the maximum variation of RB to less than 10° over 3 m, and the sum of clockwise (+) and counterclockwise (−) rotations to less than 5° over 3 m. At Holly, we loosened constraints to accommodate for noisier data, and limited the maximum variation to less than 20° over 3 m, and the sum of rotations to less than 10° over 3 m.
2. The larger and smaller caliper diameters (lengths of two opposing arms) must be at least 5% different from each other.
3. a.The smaller caliper diameter must be less than 1.1× the bit size to eliminate washouts.b.The smaller caliper diameter must be greater than the calculated keyseat criterion value.
4. The standard deviation of each caliper diameter must be less than 1 in (2.54 cm) over a 3-m borehole length.
5. The length of the breakout zone should be at least 3 m.

A keyseat is a common artifact in 4-arm caliper data that occurs when one arm of the tool digs in to the low side of the wellbore wall due to gravity. When a keyseat occurs, the one-sided elongation causes the tool to run off-center, and the smaller caliper arms record a non-diameter chord of the wellbore cross section that, in the absence of other deformations, is smaller than the size of the drill bit. We use the length of the elongated caliper arms to calculate the expected reduced length of the smaller caliper arms (keyseat criterion value) for a perfectly one-sided elongation. If the smaller caliper arms are less than or equal to this keyseat criterion value, the data are excluded. The fourth and fifth criteria above prevent the inclusion of noisy data and anomalous elongations to ensure that breakouts included in datasets represent only the most consistent and significant zones of elongation.

3.2. Averaging Borehole Breakouts

A mean depth value, as well as mean values for the breakout elongation orientation, borehole azimuth, and borehole deviation (measured from the vertical) are determined for each separate breakout zone. Angular statistics were determined using the method of Mardia and Jupp (1999). The primary benefit of this step is reduction in computation time. Additionally, averaging breakouts helps to deal with certain shortcomings of the 4-arm caliper tool. In cases where cable torque causes the tool to ride along one edge of the breakout, or to rotate slowly, but continuously within a breakout, averaging data points should provide a more accurate representation of the breakout's midpoint.

3.3. Determination of Best-Fit Stress Regime and S_{Hmax} Orientation

Based on computations of failure stresses, there are certain borehole orientations where breakout formation is less likely (Mastin, 1988). In fact, for a degenerate reverse faulting stress regime where the two horizontal

principal stresses are equal, breakouts are not expected in vertical wells; therefore, the analysis of data from deviated wellbores is necessary for determining the in situ stress in these cases.

We have developed a new misfit-based forward modeling technique based on Zajac and Stock (1997) that allows us to quantitatively constrain the best fit stress regime and S_{Hmax} orientation for a given area using borehole breakouts in closely spaced, differently oriented wellbores. We use the wellbore orientations (hole azimuth and deviation) at which each observed breakout occurred to calculate sets of corresponding theoretical borehole breakout orientations for a wide range of stress regimes and S_{Hmax} orientations. We then use a misfit calculation to determine the average angular misfit between each set of theoretical breakout orientations and the observed breakout orientations and select the stress regime and S_{Hmax} orientation of the misfit-minimizing set of theoretical breakouts as the best-fit stress parameters for the given dataset. Finally, we apply bootstrap resampling to the original data set and compile the misfit minimizing stress regimes and S_{Hmax} orientations for 100 resampled datasets to provide a range of high-confidence stress constraints for the region.

3.3.1. Parameterization of Stress State

The unrestricted principal stress tensor is completely described using six parameters. Three of these parameters describe the magnitudes of the principal stress components S1, S2, and S3, and the other three are the Euler angles (a, β, γ) that describe three successive rotations of the stress tensor about various axes to completely describe its orientation (Zajac, 1997). Operating under the assumption of a vertical principal stress, however, restricts rotation of the stress tensor to a single degree of freedom about the vertical, or z-axis, and we are therefore able to describe the complete stress tensor using only four parameters: the magnitudes of the three principal stresses (S_{Hmax}, S_{hmin}, and S_V) and a single Euler angle (α) which describes the clockwise rotation from north of S_{hmin} (90° from S_{Hmax}) about the vertical, or z-axis in the horizontal plane.

3.3.2. Selection of Represented Stress Regimes and Regime Orientations

The suite of discrete sets of theoretical borehole breakout orientations to which observed borehole breakout orientations are compared must represent a full range of possible stress regimes, as well as all possible horizontal stress orientations of each. To represent a full range of possible stress regimes, we allow the magnitude of each principal stress component to vary from 1.0–2.0 in increments of 0.1 such that there are 11 possible values for each. We then determine all unique numerical combinations of the three principal stress values, excluding those that are either illogical ($S_{hmin} > S_{Hmax}$) or unlikely ($S_{Hmax} = S_{hmin} = S_V$), and are left with 715 unique principal stress magnitude combinations that represent a range of normal, oblique normal, strike-slip, oblique reverse, and reverse faulting stress regimes. We then represent a suite of possible horizontal stress orientations for each regime by varying the Euler angle (α). The stress tensor exhibits twofold rotational symmetry in the horizontal plane, so we allow the Euler angle (α) to vary from 0° to 180° in 1° increments. Thus, a discrete set of theoretical borehole breakout orientations is calculated for each of the 715 principal stress magnitude combinations at 180 different horizontal stress orientations, resulting in 128,700 sets of theoretical borehole breakout orientations to which original borehole breakout orientations are compared.

3.3.3. Calculation of Theoretical Breakout Orientations

In order to properly represent the effects of each stress regime and regime orientation on arbitrarily oriented boreholes, we use tensor transformation equations from Zoback (2007) to rotate the far field principal stress tensors into the borehole coordinate system. Then, using equations developed by Hiramatsu and Oka (1962) and Fairhurst (1967), we are able to use the wellbore orientations (hole azimuth and deviation) at which observed borehole breakouts occurred to calculate the orientations at which borehole breakouts would theoretically form at the same wellbore orientations under each of the 128,700 stress conditions.

3.3.4. Misfit Calculation

Once all sets of theoretical breakout orientations have been calculated, we use an average angular misfit calculation to determine the best-fit stress regime and S_{Hmax} orientation.

$$M = \frac{1}{n} \sum_{j=1}^{n} |\theta_j - o_j|,$$

where n is the total number of observed borehole breakouts, o_j is the orientation of the jth observed breakout in degrees, and θ_j is the theoretical breakout orientation calculated for the wellbore orientation of the jth breakout for a given stress regime and regime orientation. The parameters of the set of theoretical borehole breakouts that exhibit the least angular misfit from the original set of observed borehole breakouts are then determined to represent the best-fit stress regime and S_{Hmax} orientation for the given dataset.

3.3.5. Bootstrapping of Data

In order to ensure confidence in the results of our forward modeling misfit calculation, we use bootstrap resampling to resample our original borehole breakout datasets 100 times, such that within each resampled dataset individual breakouts may be included multiple times, while others may be excluded. We then compute the best-fit stress regime and S_{Hmax} orientation of each resampled dataset. This approach allows us to determine if there are any underlying patterns in the data that may remain unresolved by only forward modeling the original dataset and provides a range of high-confidence stress constraints for the original borehole breakout dataset.

4. Results

4.1. Presentation of Borehole Breakout Orientations

Breakouts are traditionally plotted on an equal angle, lower hemisphere stereographic projection plot (Mastin, 1988). This gives a more realistic representation of the directions of all the possible drill holes and is suitable for datasets with few horizontal wells. We instead use a polar projection (Figure 5) as it gives more resolution to tell different nearly horizontal drill holes apart, which is particularly useful now that many more horizontal wells are being drilled.

Each borehole breakout is plotted as a single tick mark with the same orientation as the borehole elongation in a "looking down the borehole" system (Peška & Zoback, 1995). The location of the tick mark on the plot is determined by the borehole azimuth and deviation where the breakout occurs. Borehole deviation increases outward from the center of the plot, with data from vertical boreholes plotted at the center, and data from horizontal holes plotted on the periphery. Borehole azimuth changes radially around the plot.

4.2. Stress Ratio (ϕ) and A_ϕ

For simplicity in displaying the results, we further parameterize each of the 715 unique principal stress magnitude combinations using the stress ratio (ϕ) (Gephart & Forsyth, 1984), which is defined as

$$\phi = \frac{S_1 - S_2}{S_1 - S_3},$$

where S_1 is the maximum compressive stress, S_2 is the intermediate stress, and S_3 is the minimum compressive stress. The 715 combinations of S_{Hmax}, S_{hmin}, and S_V used in this study represent 33 unique stress ratio values between 0 and 1.0. Stress ratios close to 0 and 1.0 indicate $S_1 \sim S_2$ and $S_2 \sim S_3$, respectively. It is important to note, however, that any two principal stress magnitude combinations with the same value of ϕ may represent different faulting regimes depending on the orientations of S1, S2, and S3. Thus, values of ϕ are more descriptive when converted to A_ϕ as defined by Simpson (1997), which captures both ϕ and the style of faulting that each principal stress relative magnitude combination represents.

$$A_\phi = \begin{cases} \phi & \text{if } S_1 \text{ is most vertical (normal)} \\ 2 - \phi & \text{if } S_2 \text{ is most vertical (strike-slip)} \\ 2 + \phi & \text{if } S_3 \text{is most vertical (reverse)} \end{cases}$$

A_ϕ values from 0 to 1 represent normal faulting, values from 1 to 2 represent strike-slip, and values from 2 to 3 represent reverse faulting. A subtle point is that any two principal stress magnitude combinations with identical A_ϕ values (same ϕ and stress faulting regime), but different absolute principal stress magnitude values, may produce slightly different theoretical breakout orientations. Thus, the misfit value for a reverse faulting stress regime with $S_{Hmax} = 1.8$, $S_{hmin} = 1.4$, and $S_V = 1.0$ ($\phi = 0.5$; $A_\phi = 2.5$) may be slightly different than that from a regime with $S_{Hmax} = 1.2$, $S_{hmin} = 1.1$, and $S_V = 1.0$ ($\phi = 0.5$; $A_\phi = 2.5$) despite having identical ϕ and A_ϕ values.

4.3. Platform Gail Results

We analyzed eight deviated wells from platform Gail where recorded depths ranged from 790 to 1770 m TVD (true vertical depth) (Figures 4a, 4b, 5a, and 5b). Three of these wellbores were also logged at near-vertical deviations less than 10°, but no breakouts were identified in these well sections, as expected given a reverse faulting stress regime with nearly equal horizontal principal stresses, in which breakouts are less likely to

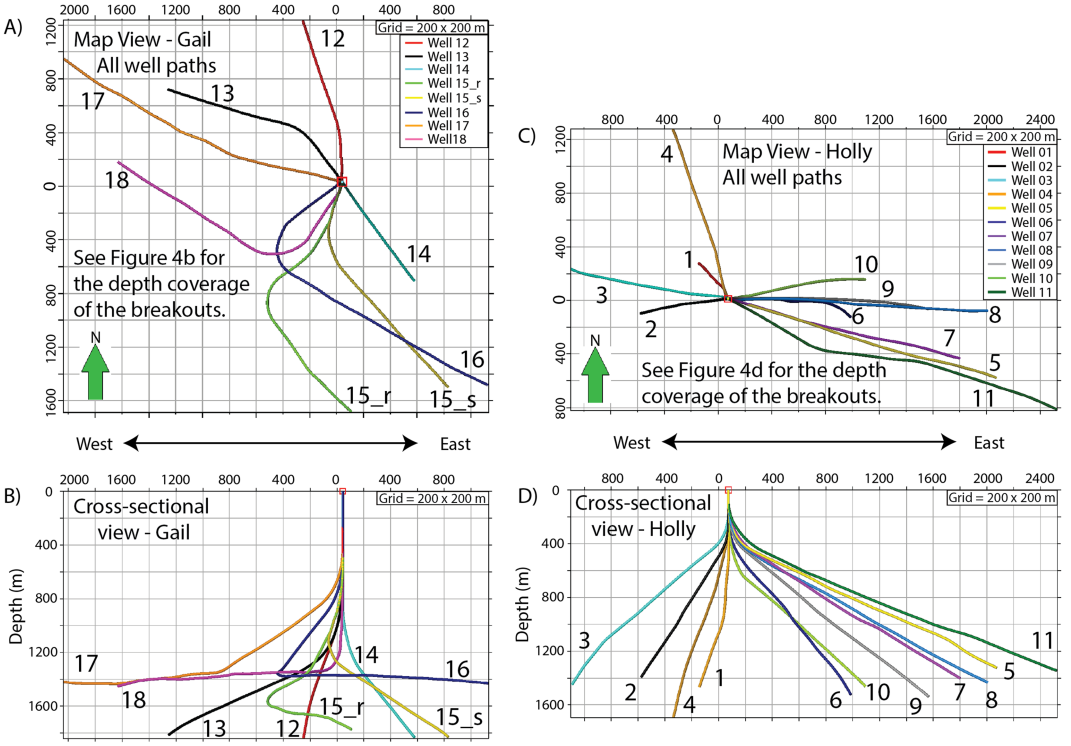

Figure 4. (a) View of platform Gail well paths from directly overhead showing the spatial extent of the wellbores. All axes are in meters. The toe of the wellbore with the furthest reach from Gail (Well 17) is 2,200 m to the NW of the platform. (b) Cross-sectional view of Gail well paths looking horizontally from S to N showing the depth coverage of the wellbores. The maximum well depth is just over 1,700 m TVD. (c) View of platform Holly well paths from directly overhead. The furthest wellbore, Well 11, reaches over 2,500 m SE from the platform. (d) View of Holly well paths looking horizontally from S to N. The maximum well depth is roughly 1,700 m TVD.

form in vertical wells. We did, however, identify six sections of breakouts in Well 14 at deviations ranging from 11° to 16° (depth range 951–986 m TVD) (near the center of Figures 5a and 5b) with a mean breakout orientation of N22°W and a standard deviation of 12° based on the method of Mardia and Jupp (1999). Studies of the effects of borehole deviation on breakout azimuth indicate that breakouts at hole deviations less than 20° in thrust faulting conditions have a greater than 88% likelihood of forming within 10° of the azimuth of the minimum horizontal stress (Mastin, 1988). Thus, these breakouts could potentially be taken to indicate an S_{Hmax} orientation of N68°E ± 12°. In addition, we also identified 142 continuous breakout zones in wellbore sections deviated from 23° to 96° (depth range 986–1652 m TVD) (Figures 5a and 5b), which, in combination with the others, allowed us to constrain both the orientations and relative magnitudes of all three principal stress components using our misfit based forward modeling technique.

Borehole breakouts in deviated wellbores beneath Gail showed some radial orientations, with sticks in the polar plots aligned radially outward from the center of the plot (Figures 5a and 5b), indicating a tendency for breakouts to form aligned with the high and low sides of the borehole. While there is some concern that these deformations could in some instances result from tool drag, measures taken during the breakout selection process ensured that deformations were stress induced and not due to other factors. Several past studies have simply excluded radial breakouts from stress analysis (e.g., Plumb & Hickman, 1985), but this practice creates gaps in breakout plots that are typically sparse to begin with and also introduces bias in the constraint of the stress ratio, ϕ, and the orientation of maximum compressive stress. Many stress states include borehole orientations at which breakouts are expected to form radially (e.g., Mastin, 1988; Peška & Zoback, 1995), and it is therefore especially important that these breakouts be selected carefully and included in stress analyses.

Misfit calculations between our original set of observed borehole breakouts and all sets of theoretical breakout orientations (Figure 6a) indicate a reverse faulting stress regime ($S_{Hmax} = 1.7$; $S_{hmin} = 1.6$; $S_V = 1.0$) with

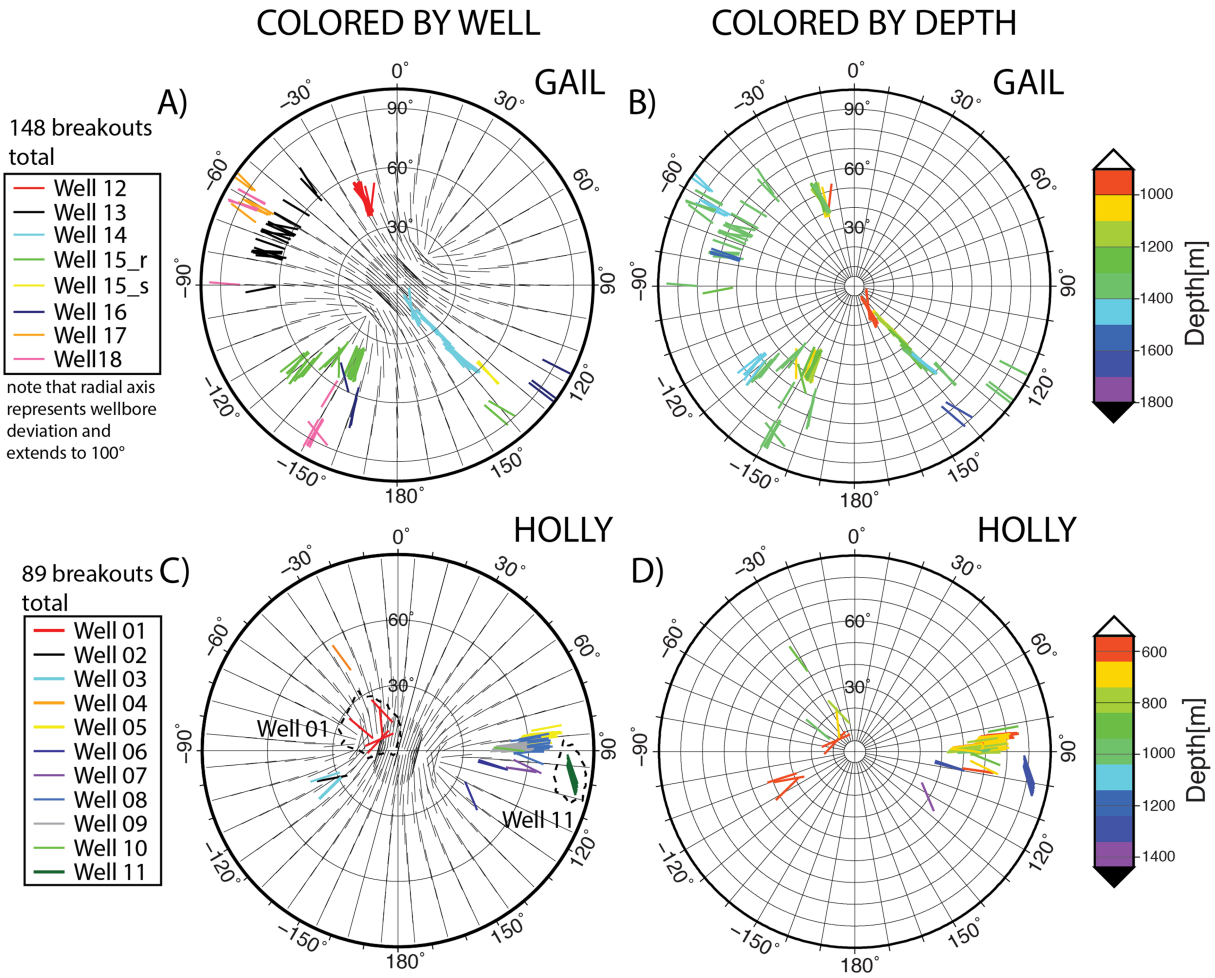

Figure 5. (a) Polar plot of platform Gail breakout orientations color-coded by individual wells plotted on top of black sticks that represent the theoretical best-fit stress state (see Figure 6). (b) Platform Gail breakout orientations with each breakout color-coded by true vertical depth. (c) Polar plot of platform Holly breakout orientations color-coded by individual wells plotted on top of black sticks that represent the theoretical pattern for the best-fit stress state (see Figure 7). Concentric grid circles represent borehole deviation at 30° intervals. (d) Polar plot of platform Holly breakouts color-coded by true vertical depth.

a stress ratio of 0.14 ($A_\phi = 2.14$) and an S_{Hmax} orientation of N45°E. Additionally, all 100 bootstrap samples of the original platform Gail data indicate a reverse faulting regime ($S_{Hmax} > S_{hmin} > S_V$). Possible stress ratios from bootstrap sample datasets ranged from 0.1 to 0.2, with a median value of 0.17 (Figure 6c), and possible S_{Hmax} orientations ranged from N40°E to N55°E with a median value of N44°E (Figure 6b). Therefore, our results from the original set of observed borehole breakouts represent very high confidence constraints on the stress field beneath platform Gail. The N68°E ± 12 S_{Hmax} orientation from the near vertical sections of Well 14 thus presents a more localized value, and the N45°E S_{Hmax} orientation from our misfit calculations is more representative of the volume sampled by all of the wells.

4.4. Platform Holly Results

We analyzed 11 deviated wells from platform Holly where recorded depths ranged from 545 to 1590 m TVD (Figures 4c, 4d, 5c, and 5d). We identified two sections of borehole breakouts in Well 01 from this platform that occurred in the near-vertical section of the well and were therefore useful in constraining the orientation of the maximum horizontal principal stress. These breakouts occurred at a mean hole deviation of 10° (depth range 557–568 m TVD) (near the center of Figures 5c and 5d) and indicated a mean S_{Hmax} orientation of N36°W with a standard deviation of 16°. We also identified three sections of borehole breakouts in this same well that occurred at deviations ranging from 15° to 20° (depth range 645–991 m TVD) (Figures 5c and 5d) and indicate a mean S_{Hmax} orientation of N57°E with a standard deviation of 24°. In addition to

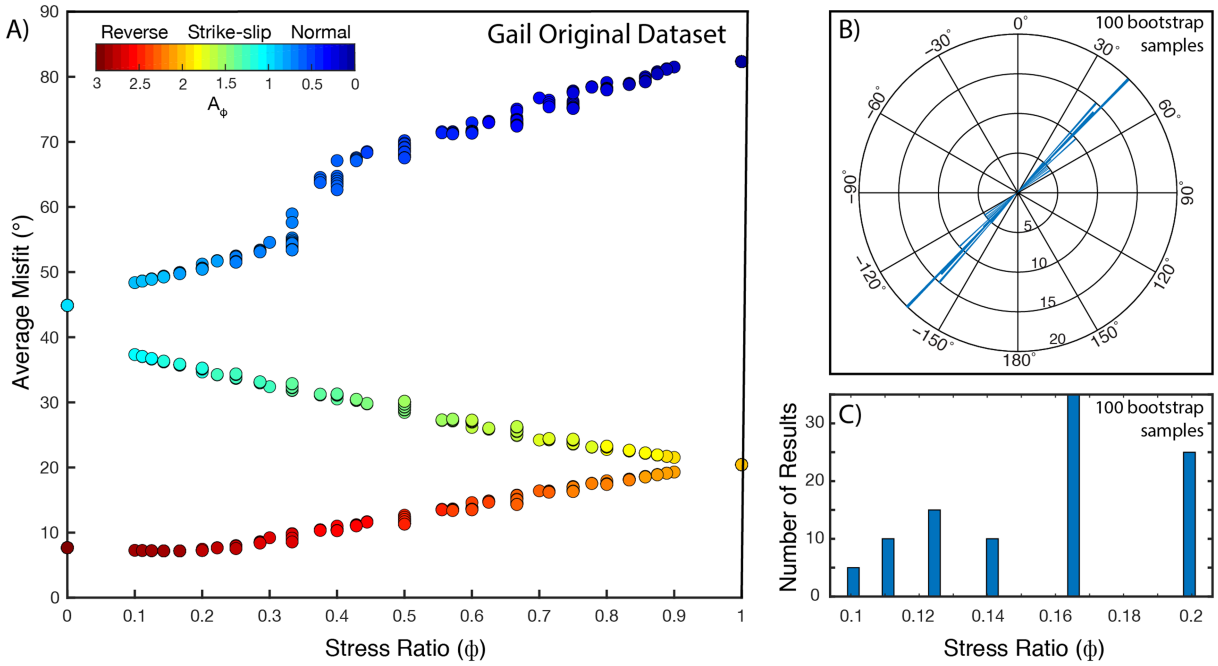

Figure 6. (a) Misfit between observed borehole breakouts at platform Gail and theoretical breakout orientations from the best-fit S_{Hmax} orientation for each of the 715 represented stress regimes. The best-fit stress state is a reverse faulting stress regime ($S_{Hmax} = 1.7$; $S_{hmin} = 1.6$; $S_V = 1.0$) with a stress ratio of 0.14 and an S_{Hmax} orientation of N45°E. (b) Rose plot of S_{Hmax} orientations of the best-fit stress regimes obtained from 100 bootstrap datasets, which ranged from N40°E to N55°E with a median of N44°E. (c) Histogram of stress ratios of best-fit stress regimes from 100 bootstrap datasets, which ranged from 0.1 to 0.2, with a median of 0.17. Gaps in the histogram are stress regimes that were not represented by the 715 relative magnitude combinations used in this study.

these 5 breakouts, we identified 84 continuous breakout zones in wellbore sections deviated from 32° to 81° (depth range 550–1405 m TVD) (Figures 5c and 5d), which we used in combination with the others to constrain both the orientations and relative magnitudes of all three principal stress components beneath the platform.

Misfit calculations using our original set of observed borehole breakouts indicate a reverse faulting stress regime ($S_{Hmax} = 2.0$; $S_{hmin} = 1.9$; $S_V = 1.0$) with a stress ratio of 0.10 and an S_{Hmax} orientation of N75°W (Figure 7a). Additionally, all 100 bootstrap samples of the original Holly data indicate a reverse faulting stress regime. Possible stress ratios from bootstrap sample datasets ranged from 0 to 0.3 with a median value of 0.1 (Figure 7c), and possible S_{Hmax} orientations ranged from N11°W to N86°W, with a median value of N74°W (Figure 7b).

In comparison with platform Gail, where a larger number of breakouts were identified at a wide range of borehole azimuths and deviations, the average angular misfit values for non-best-fit stress states at Holly increase very slowly as A_ϕ decreases from 3 to 1 (Figure 7a). The best-fit strike-slip stress regime for Holly is just 2° different from the overall best-fit regime, and the entire range of stress states with A_ϕ ranging between 1 and 3 falls within 7° average angular misfit of the overall best-fit regime. The closeness in misfit results between these regimes and the best-fit regime stems from the fact that 79 of the 89 breakouts identified occurred in wellbores that were drilled at azimuths between N81°E and N99°E (Figures 4c, 5c, and 5d). Furthermore, the majority of these breakouts formed on the high and low sides of the borehole, such that their orientations are plotted radially on the polar plot (Figures 5c and 5d).

All theoretical plots for stress regimes with A_ϕ between 1 and 3 have a range of borehole azimuths at which breakouts are expected to form radially. The width of this azimuthal range decreases from $A_\phi = 3$ (degenerate thrust), where all breakouts are expected to form radially, to $A_\phi = 1$ (transition of strike-slip to normal), where breakouts form radially regardless of deviation at only a single borehole azimuth. Thus, given mostly radial breakouts at a narrow range of borehole azimuths, a large range of stress regimes with A_ϕ ranging between 1 and 3 may exhibit relatively low misfit values at a range of S_{Hmax} orientations. This results in a

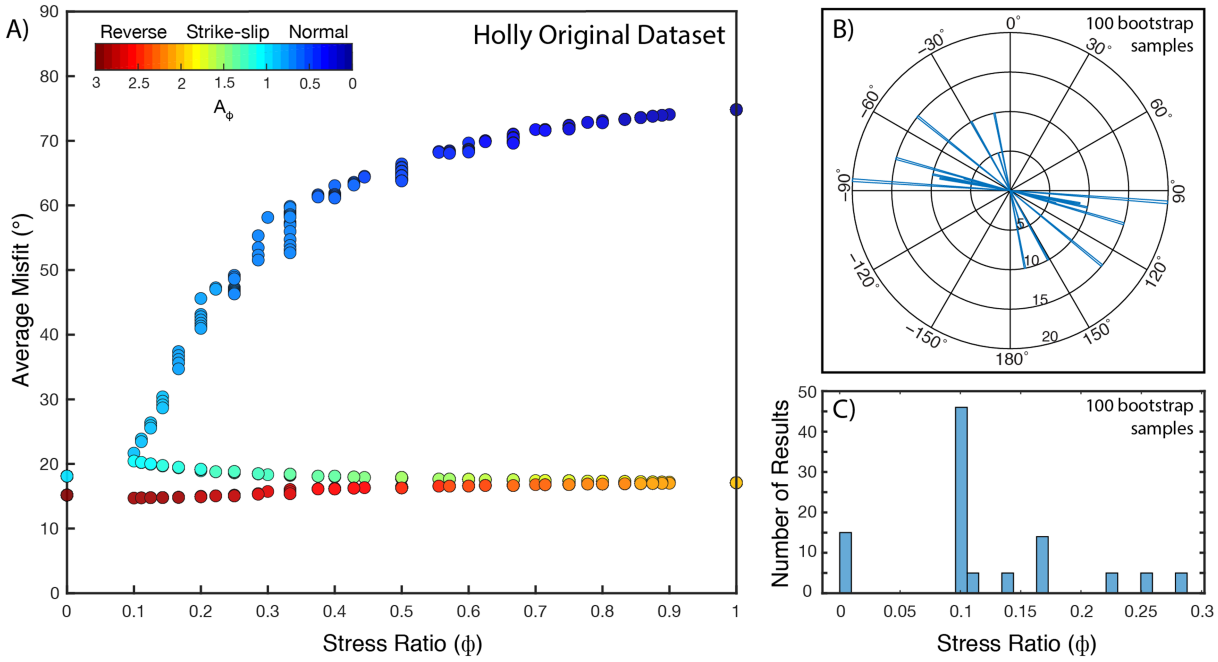

Figure 7. (a) Misfit between observed borehole breakouts at platform Holly and theoretical breakout orientations from the best-fit S_{Hmax} orientation for each of the 715 represented stress regimes. A range of low misfit values is obtained for reverse, oblique reverse, and strike-slip faulting stress regimes. In the shallow near-vertical parts of Well 01, the S_{Hmax} orientation is N36°W, and N57°E at depth (see Figures 5c and 5d). (b) Rose plot of S_{Hmax} orientations of the best-fit stress regimes obtained from 100 bootstrap resampled datasets, which ranged from N11°W to N86°W with a median of N74°W. (c) Histogram of stress ratios of best-fit stress regimes from 100 bootstrap datasets. Gaps in the histogram are stress regimes that were not represented by the 715 relative magnitude combinations used in this study.

poor constraint of the best fit stress regime and S_{Hmax} orientation at platform Holly that is, however, narrowed down to either a reverse, oblique reverse, or strike-slip faulting regime.

Well 11 breakouts, outlined with a dashed line in Figure 5c, are a notable exception in the breakout pattern at Holly. These breakouts are relatively deep (~1200 m) and are located in an isolated area where Well 11 reaches the farthest from the platform (Figure 4d). This rotation in breakout orientations points to either a change in relative stress magnitudes in that area, or a stress state where no principal stress is vertical.

5. Discussion

5.1. Platform Gail—Stress Orientations

While no other studies have analyzed borehole breakouts in the immediate vicinity of platform Gail, both Mount and Suppe (1992) and Wilde and Stock (1997) observed borehole breakouts onshore in the nearby Oxnard Plain located in the Central Ventura Basin ~20–30 km northeast of Gail (Figure 8). Neither study constrained a stress regime for their respective areas, but both were able to constrain S_{Hmax} orientations from borehole breakouts in vertical drillholes. Mount and Suppe (1992) used the borehole breakout identification criteria from Plumb and Hickman (1985). Of the wells in their dataset, the two located closest to platform Gail were Friedrich unit 3-2 and Utsaki-Burns 1 of the Oxnard Plain, which exhibited S_{Hmax} orientations of N22°E and N13°E, respectively (Figure 8). While these results are consistent with an overall NE-SW regional trend of S_{Hmax}, they are rotated 23° and 32° counterclockwise from the S_{Hmax} orientation we determined for platform Gail. This difference in orientations may reflect heterogeneity in the orientation of S_{Hmax}, but it could also be a result of the breakout identification criteria used by those authors.

Wilde and Stock (1997) modified the breakout identification criteria of Plumb and Hickman (1985) to more rigorously exclude elongations due to washouts, partial narrowing of the hole, and tool malfunctions. Additionally, they excluded all breakouts shorter than 10 ft, ensuring that only the most significant deformational trends were included in their analysis. Using these modified criteria, Wilde and Stock (1997) identified

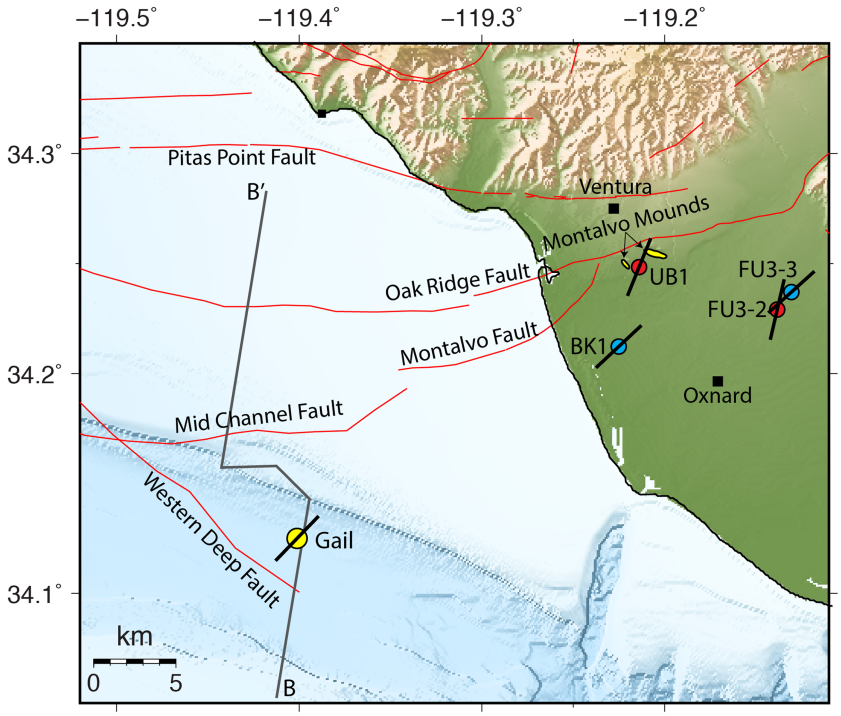

Figure 8. Map showing platform Gail (yellow circle) and onshore Oxnard Plain well locations with borehole breakout derived S_{Hmax} orientations shown with black lines. Regional scale faults are shown in red, and the path of the composite 2-D seismic profile B–B′ is shown with a grey line (see Figure 2 for the profile). Mount and Suppe (1992) Freidrich Unit 3-2 (FU3-2) and Utsaki-Burns 1 (UB1) are shown with red circles, and Wilde and Stock (1997) Ballard Kramer 1 (BK1) and Freidrich Unit 3-3 (FU3-3) wells are shown with blue circles. The NW-trending Montalvo Mounds are highlighted in yellow (Fisher et al., 2005).

borehole breakouts in two wells from the Oxnard Plain, Friedrich Unit 3-3 and Ballard Kramer 1, which indicated S_{Hmax} orientations of N48°E and N47°E, respectively (Figure 8). Their results are within 3° and 2° of the S_{Hmax} orientation that we have constrained beneath platform Gail, indicating that the orientation of maximum horizontal compressive stress is potentially laterally continuous throughout the area that includes both Gail and the Oxnard Plain, but the stress regime may be different.

5.2. Platform Gail—Relationship to Local Structures

The S_{Hmax} orientations constrained beneath platform Gail and the Oxnard plain are further supported by both local and regional structural trends present at each of these locations. Platform Gail sits just north of the S-dipping, NW-striking Western Deep fault (Figures 1b and 8), a blind, regional scale thrust fault that tips out with shallow deformation expressed as folding (Figure 2c). Fold expression on the sea floor indicates that this fault is likely still active. On a more local scale, wells from the platform target the Sockeye anticline structure, which is a broad, NW-trending, doubly plunging anticline bounded to both the north and southwest by S-dipping, NW-striking thrust faults (Figure 2b) (Sankur et al., 1990). Thus, our assertion of a reverse faulting stress regime with an S_{Hmax} orientation of N45°E is consistent with the local compressive structures of the Sockeye anticline, which are reflective of the deeper regional trend of the Western Deep fault.

The wells from previous studies discussed above target two separate oil fields within the Oxnard Plain, with each study containing one well from each field. Friedrich Unit 3-3 from Wilde and Stock (1997) and Friedrich Unit 3-2 from Mount and Suppe (1992) both target the Santa Clara Avenue oil field, while Wilde and Stock (1997) Ballard Kramer 1 and Mount and Suppe (1992) Utsaki-Burns 1 both target the West Montalvo oil field. The Santa Clara Avenue oil field is a stratigraphically trapped reservoir (DOGGR, 1992) and therefore does not contain any major structural trends with which the orientation of maximum compressive stress can be correlated. However, the West Montalvo oil field wells target the E-W trending Montalvo anticline, which is bound to the north by a steeply SE-dipping, NE-striking segment of the Oak

Ridge Fault, and is cut by a steeply N-dipping, NE-striking growth fault called the Montalvo fault (Figure 8) (Johnson et al., 2017; Yeats, 1976).

While both studies were unable to constrain the stress regime beneath their West Montalvo wells, several studies have proposed that the Montalvo Mounds, which are two short-wavelength pressure mounds overlying the buried eastern tip of the Oak Ridge fault, may indicate recent and ongoing left or left-oblique slip along the Oak Ridge fault, Montalvo fault, and other fault splays in the area (Fisher et al., 2005; Johnson et al., 2017; Yeats, 1976). The Montalvo Mounds trend NW-SE and are potentially cored by shallow thrust faults (Fisher et al., 2005). In a strike-slip stress regime, the NE-SW orientations of S_{Hmax} from both studies are consistent with these local structural trends in that S_{Hmax} is oriented at a low angle to the fault planes of the potentially strike-slip or oblique reverse, NE-striking Oak Ridge and Montalvo faults and is oriented at a high angle to the fold axis of the contractive NW-trending Montalvo Mounds.

In the case of Gail, the area sampled by the wells is 3.2 km × 2.9 km (Figures 2a and 4), which we take to at least represent the stress regime of the Sockeye anticline structure shown in Figure 2b. However, we are cautious about ubiquitously extending Gail's stress regime as far as the Oxnard plains even though S_{Hmax} in this larger region shows similar orientations, because results in the Oxnard Plain indicate in part an oblique- or strike-slip regime. We also note that stress regimes determined in the Yang and Hauksson (2013) focal mechanism inversion study show high lateral variability in Southern California. Their S_{Hmax} orientations from focal mechanisms also show an ~30° variation between the region near Gail and the nearby onshore region, a larger variability than in Wilde and Stock (1997) and the current study.

5.3. Platform Holly—Lateral and Depth Variations of SHmax

At platform Holly, breakouts in near vertical wellbore sections of Well 01 indicate two distinctly different S_{Hmax} orientations at different depths. At shallow depths from 557 to 568 m TVD, two breakouts indicate a mean S_{Hmax} orientation of N36°W ± 16°, and three breakouts occurring at depths from 645 to 991 m TVD indicated a mean S_{Hmax} orientation of N57°E ± 24°. Of the two S_{Hmax} orientations, the deeper orientation of N57°E occurs over a larger depth interval and is most consistent with previous results from borehole breakouts in the Santa Barbara Channel and the nearest WSM focal mechanism (FM1) (Figure 9). This orientation is therefore taken to represent the dominant S_{Hmax} trend for Holly.

The shallower S_{Hmax} orientation represents a 93° counterclockwise rotation of S_{Hmax}. Several previous borehole breakout studies have noted similar scale rotations of S_{Hmax}. Rajabi et al. (2017) identified a 90° rotation of borehole breakouts over a 4 m interval in the Clarence-Moreton Basin, Australia. Lin et al. (2010) identified cases of 90° borehole breakout rotations occurring both abruptly and gradually over greater borehole lengths ~2 km from the surface rupture of the 1999 Mw7.6 Chi-Chi earthquake. Shamir and Zoback (1992) observed depth-dependent variations in breakout azimuths from a few degrees to as much as 100° over depth intervals of several centimeters to hundreds of meters ~4.2 km from the San Andreas fault in Southern California. Each of these studies, and numerous others that also observed various scales of S_{Hmax} rotations occurring with depth in individual wellbores, have attributed these rotations to the presence of faults, fractures, or density contrasts, which cause localized perturbations in the stress field. Observations from both Rajabi et al. (2017) and Lin et al. (2010) indicate that abrupt changes of S_{Hmax} are more consistent with the presence of faults, while gradual rotations of S_{Hmax} are more consistent with the presence of fractures. Unfortunately, however, there is a 75 m gap between the two breakout zones that occur in Well 01, and in the absence of borehole televiewer logs, lithological logs, or information on local scale structures near Holly, we are unable to identify the cause of this rotation.

In addition, the single earthquake focal mechanism in the WSM database (WSM FM1) from a M_w 4.9 thrust faulting earthquake that occurred at 8 km depth just 3.2 km from Holly indicates a N30°E orientation of S_{Hmax}. The Dreyfus #84 well (D84) from Wilde and Stock (1997) located onshore, roughly 10 km north of platform Holly, shows an S_{Hmax} orientation of N2°E (Figure 9). The relatively short distance between the Dreyfus #84 well and Holly, however, crosses highly complex structures, and there are several faults of various orientations in this small area (Figures 1, 3, and 9), most notably those of the Pitas Point-North Channel-Red Mountain fault system. Additionally, breakouts in Dreyfus #84 occurred only at shallow depths of 284–558 m, while the Wilde and Stock (1997) Holly breakouts occurred at 488–2790 m depths, and ours occurred at 545–1590 m depths. Therefore, while the Dreyfus #84 results provide an accurate

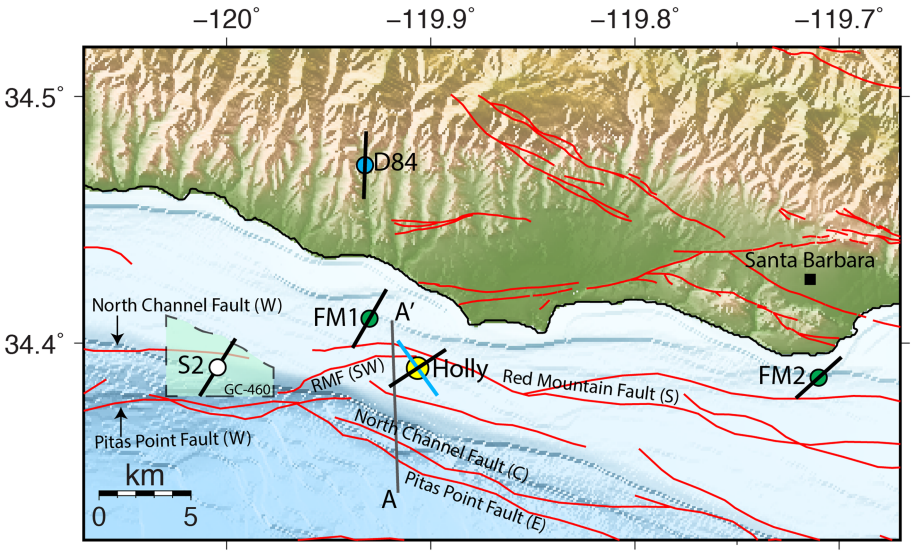

Figure 9. Map showing the locations of platform Holly (yellow circle), Heck and Edwards (1998) Samedan #2 well (S2) (white circle) of the Gato Canyon lease 460, Wilde and Stock (1997) Dreyfus #84 well (D84) (blue circle), and two single earthquake focal mechanisms from the World Stress Map database (FM1 and FM2) (green circles) (Heidbach et al., 2010), with S_{Hmax} orientations from each stress indicator shown with black lines. The blue line at platform Holly represents an S_{Hmax} of N36°W at 557–568 m TVD and the black line represents an S_{Hmax} of N57°E at 645–991 m TVD. FM1 was a M_w 4.9 thrust earthquake that occurred at 8 km depth in 2013, and FM2 was a M_w 5.9 thrust earthquake that occurred at 11.3 km depth in 1978. Regional scale faults are shown in red, and the location of the Gato Canyon 2-D seismic profile A–A′ is shown with a grey line (see Figure 3 for the profile).

representation of the orientation of S_{Hmax} beneath the onshore location of that well, the breakouts from our Well 01 likely better represent the orientation of S_{Hmax} beneath platform Holly itself.

Our results, when combined with those of previous studies show a high degree of spatial heterogeneity in the orientations of S_{Hmax} within a 10 km × 10 km area proximate to faults of the Pitas Point-North Channel-Red Mountain fault system. A 25° difference in S_{Hmax} orientations exists between our N57°E result at platform Holly and the Samedan #2 well located ~10 km to the west, and a 27° difference exists between our results and WSM FM1 located 3.2 km to the NE. Furthermore, we see a 55° difference in the S_{Hmax} orientation between platform Holly and the onshore Dreyfus #84 well.

5.4. Platform Holly—Relationship of Stress Regime to the Fault Systems

Platform Holly, the Samedan #2 well, and WSM FM1 are all located offshore along the Pitas Point-North Channel-Red Mountain fault systems (Sorlien et al., 2016; Sorlien & Nicholson, 2015). However, there is a significant boundary near platform Holly at which each of these faults exhibit significant changes in orientation. Beneath the platform, the two deepest faults of this system, the Pitas Point and North Channel faults, show around a 25° clockwise change in strike, which is accomplished by a geometric segment boundary in the North Channel fault, and a continuous double bend in strike of the Pitas Point fault (Sorlien et al., 2015; Sorlien & Nicholson, 2015) (Figure 3). At this same location, there is also a significant segment boundary and change in strike of the steeply dipping Red Mountain fault, which is divided into two segments that overlap just west of the platform (Figure 3a). The Red Mountain South segment, located mostly east of Holly, strikes nearly E-W, and the Red Mountain SW segment, located just west of Holly, strikes NE.

Some studies have suggested that a component of left-lateral strike-slip motion is expected along the major faults of these fault systems (Sorlien et al., 2015; Sorlien & Nicholson, 2015). Our results, and those from the Samedan #2 well, are consistent with the complex geometries of and proposed component of left-lateral slip along these faults. The Samedan #2 well is located between two E-W trending segments of the Pitas Point and North Channel faults. The S_{Hmax} orientation of N32°E determined at this location is at a high angle, but not perpendicular to both of these fault segments, and is therefore consistent with a component of left-lateral slip along them. Finally, a component of left-lateral motion across the 25° clockwise bend in

the strike of the Pitas Point and North Channel faults, located near Holly, could potentially induce compressive shortening in that region, which would be consistent with a local reverse faulting stress regime that we have constrained.

However, the S_{Hmax} orientation of N2°E at the Dreyfus #84 well is oriented nearly perpendicular to the nearby onshore faults. Thus, the interpreted rotation in the orientation of S_{Hmax} between the offshore and onshore regions could potentially indicate that a transition to a less oblique and more reverse faulting regime occurs in the 10 km distance north of the channel faults.

Heterogeneity in the crustal stress field plays an important role in determining the tendency of faults to slip (Morris et al., 1996). The observed stress heterogeneity in the channel may hold significant implications for the debate regarding the seismic hazard potential of the fault systems. In Well 01 from our dataset alone, we identify an ~90° rotation of S_{Hmax}, which shows that there is stress heterogeneity with depth at platform Holly, likely due to fault interactions or fractures. Additionally, our results, when combined with the N2°E S_{Hmax} orientation from Wilde and Stock (1997), the N32°E S_{Hmax} orientation from Heck and Edwards (1998), and the N30°E S_{Hmax} orientation from the WSM FM1 show spatial heterogeneity in S_{Hmax} orientations within a 10 km × 10 km region of high structural complexity in the northern Santa Barbara Channel.

6. Conclusions

We provide new constraints on crustal stress beneath the Santa Barbara Channel that are important for modeling earthquake rupture and ground motions in the region. Our approach is based on a misfit based forward modeling technique for borehole breakouts from deviated wells and improved borehole breakout selection criteria.

Our constraints at platform Gail indicate the presence of a reverse faulting stress regime with a N45°E orientation of S_{Hmax} (bootstrap confidence range N40°E-N55°E). These results are consistent with local structures, which reflect deeper regional scale trends, and are also in agreement with previous results in the onshore Oxnard Plain. Despite this consistency in S_{Hmax} orientations, we are cautious about ubiquitously extending Gail's reverse faulting stress regime as far as the onshore region due to prior studies indicating the possibility of a recent strike-slip regime there.

At platform Holly, we identified a reverse or oblique reverse faulting stress regime with a S_{Hmax} rotation from N36°W ± 16° to N57°E ± 24° occurring across ~100 m depth in a single well. This rotation is likely due to perturbations in the stress field that may be caused by a fault, fracture, or density contrast. These results, when combined with a prior borehole breakout study 10 km to the west, and a thrust faulting earthquake focal mechanism 3.2 km to the northwest, which indicated S_{Hmax} orientations of N32°E and N30°E, respectively, show significant heterogeneity in the orientation of S_{Hmax} along the Pitas Point-North Channel-Red Mountain fault system. Furthermore, previous borehole breakout studies onshore, roughly 10 km to the north, constrained an S_{Hmax} orientation of N2°E, which indicates significant heterogeneity in the S_{Hmax} orientations, and potentially the stress regimes between the offshore and onshore regions in this area.

In light of our results, and those of previous studies, it is not surprising that several studies comparing borehole breakout-derived stress constraints and regional focal mechanism stress inversions have identified disagreement between the two. While this disagreement may be in part due to the fact that the two datasets sample different depth intervals of the crust, we offer a further explanation that borehole breakouts are able to resolve stress heterogeneity at a scale that is not matched in focal mechanism inversions. Their sampling of the uppermost crust, where stress is more heterogeneous than at depth, therefore provides a rich dataset that should be embedded in a more homogenous regional stress field to better address how the different scales of stress heterogeneity and complexity impact dynamic rupture models of high-risk fault systems such as those of the Santa Barbara Channel.

Acknowledgments
We thank three anonymous reviewers, the Editor, Thorsten Becker, and the Editor in Chief, Claudio Faccenna, for their insightful comments and suggestions, which significantly improved this manuscript. The raw dataset of digital well curves used in this study was provided by oil companies in the Southern California area and is proprietary and subject to confidentiality agreements. The well names are anonymized. The well locations, well paths and depths, and all other information derived during the processing are presented in the paper. Figures were prepared with the Generic Mapping Tool (GMT) software (Wessel et al., 2013) and Petrel. We thank C. Sorlien, M. Kamerling, C. Nicholson, and R. Behl for sharing their work and Sorlien for compiling the seismic profiles shown in Figures 2c and 3c. We thank the Geology and Geophysics Department at Louisiana State University for supporting this project. Portions of this research were conducted with high performance computing resources provided by Louisiana State University (http://www.hpc.lsu.edu). This research was partly supported by the Southern California Earthquake Center (Contribution No. 8267). SCEC is funded by NSF Cooperative Agreement EAR-1033462 & USGS Cooperative Agreement G12 AC20038.

References

Atwater, T. (1970). Implications of plate tectonics for the Cenozoic tectonic evolution of western North America. *Geological Society of America Bulletin*, *81*(12), 3513–3536. https://doi.org/10.1130/0016-7606(1970)81[3513:IOPTFT]2.0.CO;2

Atwater, T., & Stock, J. (1998). Pacific-North American plate tectonics of the Neogene southwestern United States: An update. *International Geology Review*, *40*(5), 375–402. https://doi.org/10.1080/00206819809465216

Behl, R., C. Nicholson, C. Sorlien, J. Kennett, C. Marshall, S. H. Decasari, and D. Escobedo (2016), Chronostratigraphy of the Quaternary Santa Barbara Basin: An integrated geophysical, sedimentologic, and paleoceanographic approach, *2016 AAPG Pacific + Rocky Mountain Joint Meeting*.

Bell, J. S. (1996). In situ stresses in sedimentary rocks (Part 2): Applications of stress measurements. *Geoscience Canada*, *23*(3), 135–153.

Bell, J. S., & Gough, D. I. (1979). Northeast-southwest compressive stress in Alberta evidence from oil wells. *Earth and Planetary Science Letters*, *45*(2), 475–482. https://doi.org/10.1016/0012-821X(79)90146-8

Carminati, E., Scrocca, D., & Doglioni, C. (2010). Compaction-induced stress variations with depth in an active anticline: Northern Apennines, Italy. *Journal of Geophysical Research*, *115*, B02401. https://doi.org/10.1029/2009JB006395

Crouch, J. K., & Suppe, J. (1993). Cenozoic tectonic evolution of the Los Angelas basin and inner California borderland: A model for core complex-like crustal extension. *Geological Society of America Bulletin*, *105*(11), 1415–1434. https://doi.org/10.1130/0016-7606(1993)105<1415:LCTEOT>2.3.CO;2

Day-Lewis, A., Zoback, M., & Hickman, S. (2010). Scale-invariant stress orientations and seismicity rates near the San Andreas Fault. *Geophysical Research Letters*, *37*, L24304. https://doi.org/10.1029/2010GL045025

Dickinson, W. R. (1996), Kinematics of transrotational tectonism in the California Transverse Ranges and its contribution to cumulative slip along the San Andreas transform fault system, Geol. Soc. Am. Special Paper 305.

DOGGR (1992), Southern, Central Coastal, and Offshore California oil and gas fields, California Oil and Gas Fields, 2, 645.

Fairhurst, C. (1967), Methods of determining in-situ rock stresses at great depths, Missouri River Division, US Army, Corps of Engineers.

Fisher, M. A., Greene, H. G., Normark, W. R., & Sliter, R. W. (2005). Neotectonics of the offshore Oak Ridge fault near Ventura, Southern California. *Bulletin of the Seismological Society of America*, *95*(2), 739–744. https://doi.org/10.1785/0120040126

Gephart, J. W., & Forsyth, D. W. (1984). An improved method for determining the regional stress tensor using earthquake focal mechanism data: Application to the San Fernando Earthquake Sequence. *Journal of Geophysical Research*, *89*(B11), 9305–9320. https://doi.org/10.1029/JB089iB11p09305

Hadley, D., & Kanamori, H. (1977). Seismic structure of the Transverse Ranges, California. *Geological Society of America Bulletin*, *88*(10), 1469–1478. https://doi.org/10.1130/0016-7606(1977)88<1469:SSOTTR>2.0.CO;2

Hardebeck, J., Aagard, B., Becker, T., Shaw, B., & Shaw, J. (2012). SCEC community workshop: Community stress model. *Southern California Earthquake Center*. Los Angeles, CA. https://www.scec.org/workshops/2012/csm

Hardebeck, J., & Hauksson, E. (2001). Crustal stress field in Southern California and its implications for fault mechanics. *Journal of Geophysical Research*, *106*(B10), 21,859–2,1882. https://doi.org/10.1029/2001JB000292

Hauksson, E., Andrews, J., Plesch, A., Shaw, J. H., & Shelly, D. R. (2016). The 2015 Fillmore earthquake swarm and possible crustal deformation mechanisms near the bottom of the Eastern Ventura basin, California. *Seismological Research Letters*, *87*(4), 807–815. https://doi.org/10.1785/0220160020

Heck, R. G., and E. B. Edwards (1998), Gato Canyon Field, Santa Barbara Channel, California, American Association of Petroleum Geologists, 293-300.

Heidbach, O., Tingay, M., Barth, A., Reinecker, J., Kurfeß, D., & Müller, B. (2010). Global crustal stress pattern based on the World Stress Map database release 2008. *Tectonophysics*, *482*(1-4), 3–15.

Hiramatsu, Y., and Y. Oka (1962), Analysis of stress around a circular shaft or drift excavated in ground in a three dimensional stress state, Mem. Fac. Eng., Kyoto Univ., 24, 56-76.

Hubbard, J., Shaw, J. H., Dolan, J., Pratt, T. L., McAuliffe, L., & Rockwell, T. K. (2014). Structure and seismic hazard of the Ventura Avenue anticline and Ventura fault, California: Prospect for large, multisegment ruptures in the western Transverse Ranges. *Bulletin of the Seismological Society of America*, *104*(3), 1070–1087.

Ingle, J. C. (1980). Cenozoic paleobathymetry and depositional history of selected sequences within the Southern California Continental Borderland. *Cushman Foundation Special Publication*, *19*, 163–195.

Jennings, C. W., and W. A. Bryant (2010), Fault activity map of California: California Geological Survey Geologic Data Map 2, scale 1:750,000.

Johnson, S. Y., Hartwell, S. R., Sorlien, C. C., Dartnell, P., & Ritchie, A. C. (2017). Shelf evolution along a transpressive transform margin, Santa Barbara Channel, California. *Geosphere*, *13*(6), 2041–2077.

Kamerling, M. J., & Luyendyk, B. P. (1985). Paleomagnetism and neogene tectonics of the Northern Channel Islands, California. *Journal of Geophysical Research*, *90*(B14), 12,485. https://doi.org/10.1029/JB090iB14p12485

Kerkela, S., & Stock, J. M. (1996). Compression directions north of the San Fernando Valley determined from borehole breakouts. *Geophysical Research Letters*, *23*(23), 3365–3368. https://doi.org/10.1029/96GL03054

Larsen, S. C., Agnew, D. C., & Hager, B. H. (1993). Strain accumulation in the Santa Barbara Channel 1970-1988. *Journal of Geophysical Research*, *98*(B2), 2119–2133. https://doi.org/10.1029/92JB02043

Larson, K. M., & Webb, F. H. (1992). Deformation in the Santa Barbara Channel from GPS measurements. *Geophysical Research Letters*, *19*(14), 1491–1494. https://doi.org/10.1029/92GL01485

Lin, W., Yeh, E.-C., Hung, J.-H., Haimson, B., & Hirono, T. (2010). Localized rotation of principal stress around faults and fractures determined from borehole breakouts in hole B of the Taiwan Chelungpu-fault Drilling Project (TCDP). *Tectonophysics*, *482*(1-4), 82–91. https://doi.org/10.1016/j.tecto.2009.06.020

Liu, D., & Duan, B. (2018). Scenario earthquake and ground-motion simulations in North China: Effects of heterogeneous fault stress and 3D basin structure. *Bulletin of the Seismological Society of America*, *108*(4), 2148–2169. https://doi.org/10.1785/0120170374

Liu, D., B. Duan, and B. Luo (2016), Stress heterogeneity at restraining double bends over multicycles and its effect on rupture propagation in 3D, SCEC Annual Meeting 2016.

Lozos, J. C., Oglesby, D. D., Brune, J. N., & Olsen, K. B. (2015). Rupture and ground-motion models on the northern San Jacinto fault, incorporating realistic complexity. *Bulletin of the Seismological Society of America*, *105*(4), 1931–1946.

Luttrell, K. M., and J. L. Hardebeck (2017), Borehole breakouts versus earthquake focal mechanisms as stress field orientation indicators in Southern California: Should we agree to disagree, *2017 SCEC Annual Meeting*.

Malinverno, A., Saito, S., & Vannucchi, P. (2016). Horizontal principal stress orientation in the Costa Rica Seismogenesis Project (CRISP) transect from borehole breakouts. *Geochemistry, Geophysics, Geosystems*, *17*, 65–77. https://doi.org/10.1002/2015GC006092

Mardia, K. V., & Jupp, P. E. (1999). *Directional statistics*. London: Academic Press Inc.

Marshall, C. J. (2012), Sedimentation in an active fold and thrust belt from 1 Ma to present, Santa Barbara Channel, California, MS thesis, 77 pp, Cal State Long Beach.
Marshall, S., Funning, G., & Owen, S. (2013). Fault slip rates and interseismic deformation in the western Transverse Ranges, California. *Journal of Geophysical Research: Solid Earth*, *118*, 4511–4534. https://doi.org/10.1002/jgrb.50312
Mastin, L. (1988). Effect of borehole deviation on breakout orientations. *Journal of Geophysical Research*, *93*(B8), 9187. https://doi.org/10.1029/JB093iB08p09187
Montone, P., Mariucci, M. T., & Pierdominici, S. (2012). The Italian present-day stress map. *Geophysical Journal International*, *189*(2), 705–716. https://doi.org/10.1111/j.1365-246X.2012.05391.x
Morris, A., Ferrill, D. A., & Henderson, D. B. (1996). Slip-tendency analysis and fault reactivation. *Geology*, *24*(3), 275–278. https://doi.org/10.1130/0091-7613(1996)024<0275:STAAFR>2.3.CO;2
Mount, V. S., & Suppe, J. (1992). Present-day stress orientations adjacent to active strike-slip faults: California and Sumatra. *Journal of Geophysical Research*, *97*(B8), 11,995. https://doi.org/10.1029/92JB00130
Nicholson, C. (2017). Continuing to evaluate 3D fault geometry in special fault study areas and to update & improve the SCEC community fault model, 2016 SCEC Annual Report, 16065, 8 pp.
Nicholson, C., Sorlien, C. C., Atwater, T., Crowell, J. C., & Luyendyk, B. P. (1994). Microplate capture, rotation of the western transverse ranges, and initiation of the San Andreas transform as a low angle fault system. *Geology*, *22*(6), 491–495. https://doi.org/10.1130/0091-7613(1994)022<0491:MCROTW>2.3.CO;2
Peška, P., & Zoback, M. D. (1995). Compressive and tensile failure of inclined well bores and determination of in situ stress and rock strength. *Journal of Geophysical Research*, *100*(B7), 12,791–12,811. https://doi.org/10.1029/95JB00319
Pinter, N., C. C. Sorlien, and A. Scott (1998), Late Quaternary faulting and folding on Santa Cruz Island, California, Weigland P., ed, Contributions to the Geology of the Northern Channel Islands: Pacific Section, American Association of Petroleum Geologists, 111-122.
Plumb, R. A., & Hickman, S. H. (1985). Stress-induced borehole elongation: A comparison between the four-arm dipmeter and the borehole televiewer in the Auburn Geothermal Well. *Journal of Geophysical Research*, *90*(B7), 5513–5521. https://doi.org/10.1029/JB090iB07p05513
Qian, W., & Pedersen, L. B. (1991). Inversion of borehole breakout orientation data. *Journal of Geophysical Research*, *96*(B12), 20,093–20,107.
Rajabi, M., Tingay, M., King, R., & Heidbach, O. (2017). Present-day stress orientation in the Clarence-Moreton Basin of New South Wales, Australia: A new high density dataset reveals local stress rotations. *Basin Research*, *29*, 622–640. https://doi.org/10.1111/bre.12175
Rivera, L., & Kanamori, H. (2002). Spatial heterogeneity of tectonic stress and friction in the crust. *Geophysical Research Letters*, *29*(6), 1088. https://doi.org/10.1029/2001GL013803
Rockwell, T., K. Wilson, L. Gamble, M. Oskin, and E. Haaker (2014), Great earthquakes in the western Transverse Ranges of Southern California on the Pitas Point-Ventura thrust system, 5th International INQUA Meeting on Paleoseismology, Active Tectonics and Archeoseismology (PATA).
Roten, D., Olsen, K. B., Day, S. M., Cui, Y., & Fäh, D. (2014). Expected seismic shaking in Los Angeles reduced by San Andreas fault zone plasticity. *Geophysical Research Letters*, *41*, 2769–2777. https://doi.org/10.1002/2014GL059411
Ryan, K. J., Geist, E. L., Barall, M., & Oglesby, D. G. (2015). Dynamic models of an earthquake and tsunami offshore Ventura, California. *Geophysical Research Letters*, *42*, 6599–6606. https://doi.org/10.1002/2015GL064507
Sankur, V., L. S. Weber, and L. O. Masoner (1990), Development of Sockeye field in offshore California: A case history, Society of Petroleum Engineers, SPE 20047, 305-315.
Seeber, L., & Sorlien, C. C. (2000). Listric thrusts in the western Transverse Ranges, California. *GSA Bulletin*, *112*(7), 1067–1079.
Shamir, G., & Zoback, M. D. (1992). Stress orientation profile to 3.5 km depth near the San Andreas Fault at Cajon Pass, California. *Journal of Geophysical Research*, *97*(B4), 5059. https://doi.org/10.1029/91JB02959
Shaw, J. H., & Suppe, J. (1994). Active faulting and growth folding in the eastern Santa Barbara Channel, California. *Geological Society of America Bulletin*, *106*, 607–626.
Sibson, R. H. (2004). Frictional mechanics of seismogenic thrust systems in the upper continental crust—Implications for fluid overpressures and redistribution. *AAPG Memoir*, *82*, 1–17.
Simpson, R. W. (1997). Quantifying Anderson's fault types. *Journal of Geophysical Research*, *102*(B8), 17,909–17,919. https://doi.org/10.1029/97JB01274
Snee, J.-E. L., and M. Zoback (2018), State of stress in the Permian Basin, Texas and New Mexico: Implications for induced seismicity, The Leading Edge, Special Section: Induced Seismicity, 810-818.
Sorlien, C. C., Bennett, J. T., Cormier, M.-H., Campbell, B. A., Nicholson, C., & Bauer, R. L. (2015). Late Miocene–Quaternary fault evolution and interaction in the Southern California Inner Continental Borderland. *Geosphere*, *11*(4), 1111–1132. https://doi.org/10.1130/GES01118.1
Sorlien, C. C., and M. J. Kamerling (2000), Fault displacement and fold contraction etimated by unfolding Quaternary strata, onshore and offshore Ventura basin, California, USGS Technical Report, 18 pages.
Sorlien, C. C., and C. Nicholson (2015), Post-1 Ma deformation history of the Pitas Point-North Channel-Red Mountain fault system and associated folds in Santa Barbara Channel, California, USGS Technical Report, https://earthquake.usgs.gov/cfusion/external_grants/reports/G14AP00012.pdf, 24 pages.
Sorlien, C. C., C. Nicholson, R. J. Behl, and M. J. Kamerling (2016), Displacement direction and 3D geometry for the south-directed North Channel-Pitas Point fault system and north-directed ramps, decollements, and other faults beneath Santa Barbara Channel, SCEC Annual Meeting 2016.
Sylvester, A. G., Scholz, C. H., & Smith, S. W. (1970). Earthquake swarm in the Santa Barbara Channel, California, 1968. *Bulletin of the Seismological Society of America*, *60*(4), 1047–1060.
Vedder, J. G., H. C. Wagner, and J. E. Schoellhamer (1969), Geologic framework of the Santa Barbara Channel region, Geological Survey Professional Paper, 679-A, 1-11.
Wallace, T. C., Helmberger, D. V., & Ebel, J. E. (1981). A broadband study of the 13 August 1978 Santa Barbara Earthquake. *Bulletin of the Seismological Society of America*, *71*(6), 1701–1718.
Wessel, P., Smith, W. H. F., Scharroo, R., Luis, J. F., & Wobbe, F. (2013). Generic Mapping Tools: Improved version released. *Eos, Transactions of the American Geophysical Union*, *94*(45), 409–410. https://doi.org/10.1002/2013EO450001
Wilde, M., & Stock, J. (1997). Compression directions in Southern California (from Santa Barbara to Los Angeles Basin) obtained from borehole breakouts. *Journal of Geophysical Research*, *102*(B3), 4969–4983. https://doi.org/10.1029/96JB03734

Yang, W., & Hauksson, E. (2013). The tectonic crustal stress field and style of faulting along the Pacific North America Plate boundary in Southern California. *Geophysical Journal International*, *194*(1), 100–117.

Yeats, R. S. (1976), Neogene tectonics of the central Ventura basin, California, The Neogene Symposium, 19-32.

Yeats, R. S., Huftile, G. J., & Grigsby, F. B. (1988). Oak Ridge fault, Ventura fold, and the Sisar decollement. *Geology*, *16*(12), 1112–1116. https://doi.org/10.1130/0091-7613(1988)016<1112:ORFVFB>2.3.CO;2

Zajac, B. (1997), The state of stress as inferred from deviated boreholes: Constraints on the tectonics of offshore central California and Cook Inlet, Alaska, PhD thesis, 298 pp, California Institute of Technology.

Zajac, B., & Stock, J. M. (1997). Using borehole breakouts to constrain the complete stress tensor: Results from the Sijan Deep Drilling Project and offshore Santa Maria Basin, California. *Journal of Geophysical Research*, *102*(B5), 10,083–10,100. https://doi.org/10.1029/96JB03914

Zoback, M. D. (2007). *Reservoir geomechanics*. Cambridge: Cambridge University Press. https://doi.org/10.1017/CBO9780511586477

Zoback, M. D., Barton, C. A., Brudy, M., Castillo, D. A., Finkbeiner, T., Grollimund, B. R., et al. (2003). Determination of stress orientation and magnitude in deep wells. *International Journal of Rock Mechanics and Mining Sciences*, *40*(7-8), 1049–1076. https://doi.org/10.1016/j.ijrmms.2003.07.001

Zoback, M. L. (1992). First- and second-order patterns of stress in the lithosphere: The World Stress Map Project. *Journal of Geophysical Research*, *97*(B8), 11,703. https://doi.org/10.1029/92JB00132